The electronic structure of α-Al_2O_3 grain boundaries containing reactive element segregants

Andy Paul Chen,[1,*] Arthur H. Heuer,[1,2] Michael W. Finnis,[2,3] and W. M. C. Foulkes[3]

[1] *Department of Materials Science and Engineering, Case Western Reserve University, Cleveland, OH 44106-7204, United States*
[2] *Department of Materials, Imperial College, London SW7 2AZ, United Kingdom*
[3] *Department of Physics, Imperial College, London SW7 2AZ, United Kingdom*

(Dated: September 1, 2022)

It has long been known that the addition of small quantities ("doping") of so-called reactive elements (RE) such as Y, Zr, and Hf to high-temperature Al_2O_3 scale-forming alloys improves oxidation resistance. The presence of reactive elements at grain boundaries lowers the growth rate of the α-Al_2O_3 scales, but the cause of the reduced scale growth kinetics is not fully understood. Explanations based on steric effects and explanations based on reducing the grain boundary electronic conductivity have been proposed. We have used density functional theory to study the structural and electronic properties of two $\Sigma7$ bicrystal grain boundaries containing Y, Hf, and Zr substitutional defects on Al sites. The presence of RE substitutional defects plays a minimal direct role in reducing the density of electronic states near the valence-band maximum. However, Hf^{4+} or Zr^{4+} substitutions at the grain boundary repel the positively charged oxygen vacancy V_O^{2+}. As V_O^{2+} contributes a defect state above the valence-band maximum but below the Fermi energy, this indirectly lowers the density of current carrying holes and thus the electronic conductivity of the grain boundary. Replacing Al^{3+} ions with Hf^{4+} or Zr^{4+} ions also makes the grain boundary positively charged, further reducing the hole density.

I. INTRODUCTION

The much-appreciated oxidation resistance of Ni- and Fe-based Al_2O_3 scale-forming alloys, operating at temperatures above 900°C in oxidizing ambients, originates from the growth of protective α-Al_2O_3 scales on the alloy surface. Oxidation resistance can be increased by improving scale adhesion [1] or by slowing the already slow diffusion of oxygen and Al ions across the scale [2–4]. Bearing in mind the practical importance of high-temperature alloys, it is not surprising that the study of Al_2O_3 scale formation is a lively area of materials science research.

The transport of oxygen and aluminum across the polycrystalline Al_2O_3 scale is dominated by grain boundary (GB) diffusion [2, 5]. It has been known for decades [1] that the addition of modest concentrations of so-called reactive elements (REs) such as Y, Zr, and Hf, which segregate strongly to grain boundaries (GBs), leads to scales of α-Al_2O_3 that grow more slowly and adhere better to the alloy [3]. For example, recent experiments by Chen, Gleeson and Heuer [6] reported improved oxidation resistance in γ'-Ni_3Al-based Ni-20Al-5Cr alloys upon doping with Y, Hf, and Si. Meanwhile, Wu *et al.* [7] and Cheng *et al.* [8, 9] showed that Hf and Y dopants decrease oxygen GB diffusivity in polycrystalline α-Al_2O_3.

It has often been assumed, without much justification, that the RE effect is steric in origin: the larger RE ions are supposed to inhibit scale growth by blocking the diffusion pathways of Al and oxygen along the GB [7, 10]. However, theoretical considerations and experimental observations, which we shall explore in detail in the following paragraphs, suggest that the electronic structure of polycrystalline α-Al_2O_3 may play a significant role.

It has been known since the seminal work of Wagner [11] that the growth of a protective scale by diffusive transport of ions requires a concomitant transport of electrons and/or holes across the growing scale. This is necessary for two reasons. The first is to mediate the formation and annihilation of charged Al and oxygen vacancies or interstitials at the scale-gas and scale-metal interfaces [4]. All such reactions consume or release holes or electrons. The second is to reduce the voltage that builds up across the scale as Al^{3+} ions move out, reacting with oxygen to create new α-Al_2O_3 at the scale-gas interface, and O^{2-} ions move in, reacting with Al to create new α-Al_2O_3 at the scale-metal interface. Regardless of whether oxygen or Al transport dominates, the scale-metal interface becomes negatively charged with respect to the scale-gas interface and the voltage across the scale resists further ionic diffusion. Unless electrons or holes are able to flow across the scale to neutralize the voltage, scale growth soon ceases. This idea is supported by the observation by Sheasby and Jory [12] that application of an external voltage significantly accelerates or impedes scale growth, depending on polarity, as well as the measurement of transference numbers by Balmain and Huntz [13, 14] indicating that the electronic and ionic conductivities are similar in magnitude.

Heuer *et al.* [15] recently published an in-depth computational study of the $\Sigma7\{2\bar{3}10\}\,[0001]$ ($\Sigma7a$) and $\Sigma7\{4\bar{5}10\}\,[0001]$ ($\Sigma7m$) GBs in α-Al_2O_3. Density functional theory (DFT) molecular dynamics simulations and structural relaxations were used to establish the arrange-

* andy.paul@u.nus.edu

ments of the atoms in both boundaries, after which electronic structure calculations were carried out. An important observation was that the density of localized grain-boundary electronic states near the valence band maximum (VBM) was reduced on adding an Y^0_{Al} substitutional to the $\Sigma 7m$ boundary. Since the Fermi energy of α-Al_2O_3 lies quite low in the band gap [4], the electronic contribution to the electrical conductivity is hole dominated and the reduction in the density of accessible hole states is expected to lower the electronic conductivity.

Measurements of α-Al_2O_3 bi-crystal GBs using valence electron energy-loss spectroscopy (EELS) by Wei *et al.* [16] revealed that localized electronic states bound to GBs appear at energies both above the VBM and below the conduction band minimum (CBM). The localized GB states below the CBM are unlikely to affect the electronic conductivity because they lie far from the Fermi energy, but the localized states near the VBM can be occupied by holes, increasing the electronic conductivity. It was these states that Heuer *et al.* found to be attenuated in an Y-doped $\Sigma 7m$ boundary.

This paper has several aims. One is to establish whether this electronic conductivity explanation for the improved oxidation resistance of Y-doped α-Al_2O_3 GBs generalizes to boundaries doped with different REs. Another is to investigate other ways in which the addition of REs may affect oxidation resistance. A third is to investigate how the electronic structure changes as the density of REs on the boundary increases. The RE coverages of 20% (Zr) or even up to 60% (Y) of a monolayer observed by Schumann *et al.* [17] and Fielitz *et al.* [18] are far from the dilute limit studied in previous DFT simulations [4].

As experimental studies employing a wider variety of RE elements and doping levels become available, it is important to identify and distinguish the various physical phenomena that together constitute the reactive element effect.

II. METHODOLOGY

Our DFT calculations used the projector augmented wave (PAW) approach as implemented in the Vienna Ab-initio Simulation Package (VASP) [19–22]. The plane-wave energy cut off was set to 550 eV, which is large enough to yield well-converged results for all systems studied. The energy convergence threshold for self-consistent electronic optimization loops was 1 meV. During structural relaxations, the atomic coordinates were updated iteratively until the forces on all atoms fell below $0.05\,\mathrm{eV/\AA}$. Calculations of the total energy of a primitive trigonal unit cell of α-Al_2O_3 ($a = b = c = 5.18\,\mathrm{\AA}$; $\alpha = \beta = \gamma = 55.3°$) were well converged for a Monkhorst-Pack mesh of $5 \times 5 \times 5$ or more k points, corresponding to a k-point spacing of $0.05\,\mathrm{\AA}^{-1}$. Several local and semi-local exchange-correlation functionals were evaluated for use in structural relaxations, of which the local density approximation (LDA) gave the best agreement with experiment, producing an error of $-0.6(+0.2)\%$ in the lattice parameter $a(\gamma)$. In comparison, the error produced by the generalized gradient approximation (GGA) methods, including PBE, fall around $+1.0(+0.1)\%$ in the lattice parameter $a(\gamma)$. Local and semi-local functionals substantially underestimate the experimental band gap of 8.8eV [23, 24], but Becke's three-parameter hybrid exchange functional combined with Lee–Yang–Parr correlation (B3LYP) [25, 26] gave excellent agreement. The error of +0.1eV was significantly smaller than the errors obtained using the other semi-local and hybrid functionals tested (GGA [27], PBE [28, 29], PBE0 [30, 31], HSE03 [32–34], and HSE06 [35]).

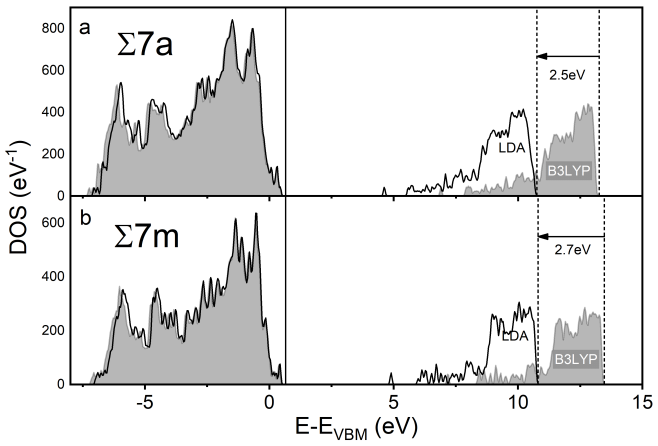


FIG. 1. Densities of States (DOS) of (a) $\Sigma 7a$ and (b) $\Sigma 7m$ boundaries calculated using density functional theory with local (LDA) and hybrid (B3LYP) exchange-correlation functionals. The LDA conduction bands are shifted down relative to the B3LYP conduction bands, as indicated by the arrows. The solid vertical line indicates the energy of the highest occupied one-electron state.

We next characterized the electronic properties of undoped $\Sigma 7a$ and $\Sigma 7m$ bicrystal GBs in α-Al_2O_3. Although manufactured GBs in a bicrystal are simplified models of random high angle GBs, they can be used to approximate the real GB environment [36]. Furthermore, the substantial difference of structure between the $\Sigma 7a$ (more disordered) and $\Sigma 7m$ (less disordered) bicrystal GBs helps us to distinguish phenomena that depend on the details of the atomic arrangement from phenomena of more general interest.

The starting structures of these pristine GBs were taken from Heuer *et al.* [15], who generated them using a carefully designed simulated-annealing procedure based on empirical interatomic potentials, followed by a final relaxation of atomic positions using forces calculated with DFT. To allow the simulation cell to be repeated periodically, it has to incorporate two parallel GBs. The $\Sigma 7a$ GB cell ($a = 12.66\,\mathrm{\AA}$, $b = 53.44\,\mathrm{\AA}$, $c = 13.07\,\mathrm{\AA}$, $\alpha = 83.4°$, $\beta = 90.0°$, $\gamma = 96.5°$) contains 336 aluminum atoms and 504 oxygen atoms, whereas the $\Sigma 7m$

GB cell ($a = 8.51$ Å, $b = 55.44$ Å, $c = 13.07$ Å, $\alpha = 78.8°$, $\beta = 59.2°$, $\gamma = 79.4°$) contains 224 aluminum atoms and 336 oxygen atoms. The densities of electronic states obtained using the LDA and B3LYP functionals are shown in Fig. 1. The LDA calculation for the $\Sigma 7a(\Sigma 7m)$ GB used a Monkhorst-Pack mesh of $5 \times 2 \times 5(7 \times 1 \times 5)$ points, corresponding to a k-point spacing smaller than $0.02\,\text{Å}^{-1}$. The B3LYP calculations used the Γ point only; this corresponds to choosing a maximum k-point spacing of $0.14\,\text{Å}^{-1}$.

In the $\Sigma 7a$ and $\Sigma 7m$ GBs, the LDA band gap is 2.5 to 2.7 eV smaller than the B3LYP band gap. In the centre of the bulk region, the B3LYP gap is very close to that of a perfect crystal, suggesting that our simulation cells are large enough to describe the bulk regions away from the GBs accurately. Apart from the difference in band gap, the LDA and B3LYP densities of states (DOS) are in excellent agreement, especially near the band edges. The DOS profile calculated with LDA also almost matches that calculated with PBE, which was used by Heuer *et al.* [15]. Furthermore, the LDA DOS does not change appreciably when the k-point spacing is increased from $<0.02\,\text{Å}^{-1}$ to $0.14\,\text{Å}^{-1}$, indicating that the relatively coarse k-point mesh used in the B3LYP calculations was adequate.

We deduce that the earlier computational study of Heuer *et al.* [15], which focused on the fine structure near the VBM, was not compromised by the use of an exchange-correlation functional known to underestimate the band gap. In our subsequent calculations of the DOS of α-Al_2O_3 GBs, the LDA exchange-correlation is employed.

A. Candidate Grain-Boundary Models

We assume that Y, Hf, and Zr dopant ions create substitutional defects by occupying Al sites in the GB regions of the models described in the previous Section. The closest 37(36) Al sites to the GB plane in the $\Sigma 7a(\Sigma 7m)$ unit cell are chosen as candidate sites for dopant substitution. This defines the region near the boundary where the crystalline structure deviates noticeably from the bulk crystal lattice.

After inserting the dopants, we relaxed the atomic positions of each dopant-containing GB to the closest local minimum. A Monkhorst-Pack mesh of $2\times1\times2$ $(3\times1\times2)$ k points was used for the $\Sigma 7a$ ($\Sigma 7m$) simulation cell; this corresponds to a maximum k-point spacing of $<0.05\,\text{Å}^{-1}$. During the relaxation, the atomic coordinates, cell volume, and cell shape were optimized. Once the relaxed boundary structure had been found, we carried out a single total energy calculation with a self-consistency convergence criterion of 1 meV.

The computational treatment of point defects requires the oxidation state of each defect to be chosen in advance, as this affects the total number of electrons in the simulation cell. The relative stabilities of defects in different oxidation states can be compared, but here we anticipate that substitutional Y will have an oxidation state +3, like Al, by preparing the simulation cell with all neutral-atom charge densities. On the other hand, we anticipate oxidation states of +4 for Hf and Zr by preparing the simulation cell with a deficit of one electron.

III. RESULTS AND DISCUSSION

A. Ground-State Atomistic GB Structures

To identify the ground-state atomistic structure for all six possible combinations of dopant (Y, Zr, Hf) and GB ($\Sigma 7a$, $\Sigma 7m$), we relax and calculate the final total energy of all 37 (for $\Sigma 7a$) or 36 (for $\Sigma 7m$ boundary) supercells that were created by replacing a single Al atom by Y, Zr or Hf. Taking the relaxed trial cell with the lowest total energy for every combination of dopant and GB yields the six ground-state configurations. We find that the ground-state locations of the Zr^{4+} and Hf^{4+} dopants are the same, while Y^{3+} occupies distinctly different sites. The most energetically stable substitutional sites are depicted in Fig. 2. Table I summarizes the oxygen coordination numbers and dopant-oxygen bond lengths as indicators of the local environment of the dopant atom at its most energetically stable substitutional site.

The behavior of Y^{3+} is attributable chiefly to its ionic radius, which exceeds that of the other RE ions by 0.19–0.20Å. The charge of the Y^{3+} ion is the same as that of the Al^{3+} ion it replaces, so creating an Y^0_{Al} substitutional defect introduces no additional local charge, rendering Coulomb effects unimportant. The trend in O-coordination is also noted; for our purposes, an O^{2-} ion and a RE ion are considered to be coordinated if the RE-O bond is shorter than the shortest Al-O bond. The Al^{3+} atom replaced by the substitutional dopant coordinates with six O^{2-} ions, but the larger ionic radius of Y^{3+} allows it to coordinate with eight O^{2-} ions in the $\Sigma 7m$ GB and seven in the $\Sigma 7a$ GB (see Fig. 2d). In addition, in the $\Sigma 7a$ boundary, the Y^{3+} ion is displaced from the corresponding Al site to help achieve this higher coordination number (see Fig. 2c). Note that eightfold-coordinated Y^{3+} ions are also characteristic of yttrium aluminum garnet (YAG; $Y_3Al_5O_{12}$).

The Hf^+_{Al} and Zr^+_{Al} substitutional defects are positively charged, making Coulomb and electronic structure effects much more important. From Fig. 3, we see that the changes in charge density associated with Hf and Zr substitutional defects are very localized on those defects, rather than distributed within the GB region or throughout the cell. This suggests that the unit cell adopted is sufficiently large that charged defects at adjacent periodic images are prevented from interacting with one another electrostatically.

Hf^{4+} and Zr^{4+} ions are smaller than Y^{3+} ions and produce less steric distortion of the GB structure (Figs. 2a

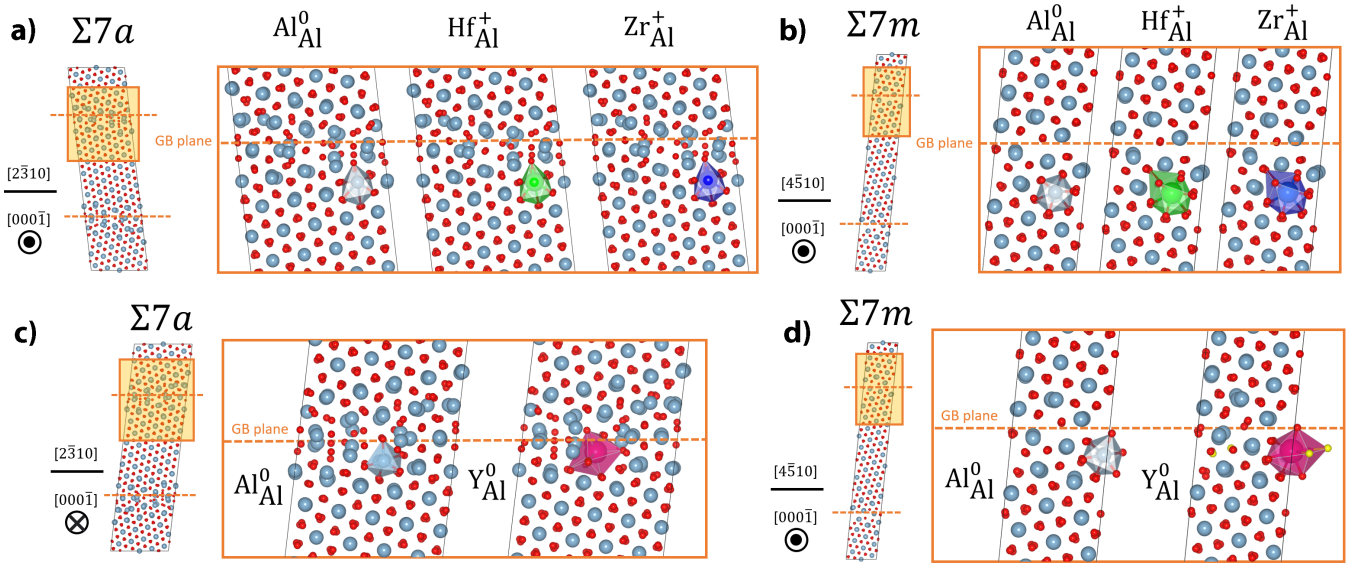


FIG. 2. Ground-state atomistic structures of pristine $\Sigma7a$ (a, c) and $\Sigma7m$ (b, d) α-Al_2O_3 GBs. Hf and Zr-doped GBs are shown in (a, b), and Y-doped GBs in (c, d). To aid comparison, the Al sites in the pristine boundaries substituted by RE ions in the doped boundaries are indicated by polyhedra. In d), the two extra oxygen ions coordinated to the Y^0_{Al} dopant are shown in yellow.

TABLE I. Coordination numbers and lengths of bonds involving dopant ions in the GB environment, based on the lowest energy candidate model in each case. The native ionic species Al^{3+} is included as a reference.

Ionic species		Y^{3+}	Hf^{4+}	Zr^{4+}	Al^{3+}
Ionic radius (Å) [37]		0.90	0.72	0.71	0.54
O–Coordination (min–max dopant–O bond length (Å))	Σ7a	7 (2.07–2.68)	6 (2.01–2.57)	6 (2.05–2.63)	6 (1.76–2.53)
	Σ7m	8 (2.13–2.99)	7 (1.95–2.66)	7 (1.96–2.61)	6 (1.81–2.17)

and 2b), but their ionic radii are nevertheless approximately 0.2 Å greater than that of Al^{3+}. In the $\Sigma7m$ GB, this small difference is sufficient to cause an extra oxygen atom to be coordinated to the relevant substitutional site (Fig. 2b).

B. Electronic Structure Effects of RE Doping in the Dilute Limit

The near-band-edge electronic densities of states of the pristine and doped $\Sigma7a$ and $\Sigma7m$ simulation cells are shown in Fig. 4. Localized GB states appear in the band gap within ∼0.5 eV of the VBM and ∼2–3 eV of the CBM.

The consequences of introducing an Y^0_{Al}, Hf^+_{Al} or Zr^+_{Al} substitutional defect may be seen by inspecting the differences between the densities of states of the GB cell with and without a RE ion. The greatest effect of introducing aliovalent dopants on the DOS is seen below the CBM. In contrast to Y^0_{Al} substitutionals, which have little effect on the near-CBM DOS, the introduction of Hf^+_{Al} and Zr^+_{Al} defects creates localized states high in the gap, in effect lowering the energy of the CBM. The energies of the localized states depend on the RE species and GB structure, with the deepest gap state lying from ∼0.5eV to ∼3.0eV below the CBM.

The density of electronic states near the VBM is much less affected by RE doping. Unlike Heuer *et al.* [15], we find that the near-VBM density of electronic states is little altered by the presence of an Y^0_{Al} substitutional defect. The effect of the other RE species, Hf and Zr, are also minimal. This contrasts with the earlier calculations of Heuer *et al.* [15], despite the fact that the GB models in the present study are constructed from their geometrically optimized pristine GB cells. This difference arises from the difference in the GB models chosen for electronic structure analysis. Rather than using the lowest-energy GB structures, as in the present study, Heuer *et al.* [15] chose a particular metastable configuration of the doped $\Sigma7m$ GB cell. The reason given was that the lowest energy configuration had a "crystal-like regularity" unconducive to Y segregation to the GB, and that a Y^0_{Al} defect in such a highly ordered GB would not produce dramatic

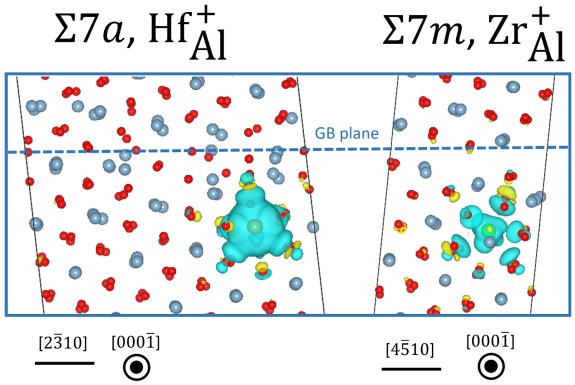


FIG. 3. Calculated changes in the charge density near substitutional defects Hf^{+}_{Al} and Zr^{+}_{Al}. The blue (yellow) isosurface indicates partial positive (negative) charge introduced by the RE species. The charge density isosurface level is $\pm 0.3 Å^{-3}$.

changes in atomic or electronic structure. However, after studying the more disordered $\Sigma 7a$ GB alongside the less disordered $\Sigma 7m$ GB, we found that the effect of Y^{0}_{Al} on near-VBM electronic states are minimal in both cases, suggesting that the degree of order of the GB atomic structure may not be as important as previously thought. Another implication is that the proposed mechanisms by Heuer *et al.* [15] are limited to the chosen metastable configuration, and cannot be applied to α-Al_2O_3 GBs in general. The present study tried substituting the single RE atom for all of the Al atoms near the grain boundary plane, following every substitution by a relaxation in DFT. For each RE species, the Al site substitution resulting in the most stable (lowest energy) cell was then selected for further electronic structure analysis.

C. Electronic Structure Effects of Quasi-Monolayer segregation of Y^{0}_{Al} at the GB

Fielitz *et al.* [18] observed that Y ions occupy up to 60% of an atomic monolayer at α-Al_2O_3 GBs. It is therefore worthwhile to study the effects of denser Y doping on the electronic structure. We consider a $\Sigma 7a$ GB simulation cell in which all of the Al sites sufficiently close to the GB plane have been replaced by Y ions. In this model, the Y coverage is 7/8 (87.5%) of a homogeneous atomic monolayer. The $\Sigma 7m$ GB has no shared Al sites situated close to the GB plane, and so is not considered in this subsection.

The coverage in our simulations is somewhat higher than Fielitz's measured values [18], but the broad consequences of heavy Y doping are clear enough. The DOS in Fig. 5 shows that the small effects seen with a single Y^{0}_{Al} substitutional defect are strongly amplified by the increase in doping, and that the reduction of the DOS at the VBM demonstrated by Heuer *et al.* [15] is once again manifest. In contrast to the previous subsection, where the DOS near the CBM was found to be little altered by the introduction of a single Y^{0}_{Al} defect, the creation of a quasi-monolayer of Y^{0}_{Al} substitutionals also introduces states below the CBM. Projection of the wave functions onto the Y sites shows that these states have substantial Y character.

D. Influence of RE Substitutional Defects on Vacancy Segregation to α-Al_2O_3 GBs

Hf- and Zr-doped GBs contain substitutional defects, Hf^{+}_{Al} and Zr^{+}_{Al}, both of which bear a single positive charge. Charge neutrality therefore requires the presence of a population of charge-compensating defects at or near the α-Al_2O_3 GB. As oxidation studies involving α-Al_2O_3 are typically conducted at elevated temperatures (up to 1600K) unfavorable to the formation of defect complexes, these charge-compensating defects normally occur as isolated point defects and are not bound to the dopants. The dominant charge-compensating defects are expected to be those with the lowest defect formation energies in bulk α-Al_2O_3 (see, for example, Figure 1(a) in [38]). In the oxidative limit, charge-compensating defects would include Al^{3+}_{i}, V^{3-}_{Al}, and V^{2+}_{O}. Here, we aim to look beyond simple RE substitutional defects and consider the role of charge-compensating defects in modulating the GB DOS. To achieve this, we consider the abundances of V^{3-}_{Al} and V^{2+}_{O} defects at the α-Al_2O_3 GB and how these are changed when a RE substitutional is also present. (As the positions of interstitial sites are poorly defined in the GB region, a systematic study of interstitial defect segregation to GB would be very difficult. We do not attempt it.)

The segregation energy of an oxygen/Al vacancy to a specific GB site is defined as the difference between the formation energy of a vacancy at the GB site and the formation energy of a vacancy in the bulk. The more negative the segregation energy, the higher the concentration of vacancies at the GB relative to the concentration in the bulk. The segregation energy of a vacancy to a specific GB site is easily calculated in DFT by comparing the total energies of two simulation cells, one with the vacancy in the bulk region and the other with the vacancy on the GB site of interest:

$$\Delta E_{\text{seg}} = E_T^{\text{def},q}(\text{GB}) - E_T^{\text{def},q}(\text{bulk}). \qquad (1)$$

Figure 6 summarizes the segregation energies of V^{3-}_{Al} and V^{2+}_{O} vacancies to the $\Sigma 7a$ and $\Sigma 7m$ GBs. The possible GB defect sites considered consisted of the ∼40 Al sites and ∼60 oxygen sites closest to the GB plane.

The mean segregation energy of V^{3-}_{Al} is close to but slightly above zero for both GBs; the median segregation energy is slightly less than zero in the $\Sigma 7m$ boundary and slightly greater than zero in the $\Sigma 7a$ boundary. Both boundaries contain Al sites with substantially negative segregation energies, suggesting that some V^{3-}_{Al} vacancies

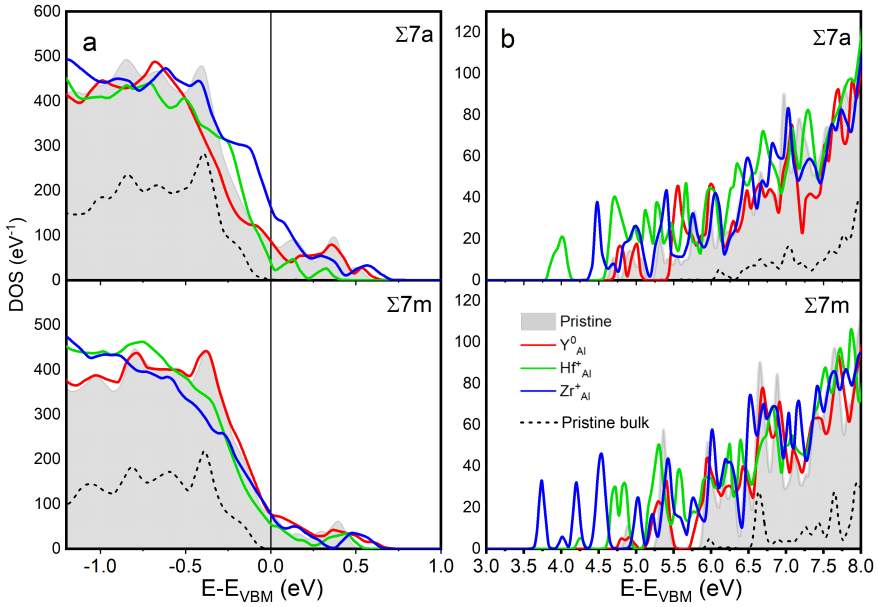


FIG. 4. The densities of states of the $\Sigma 7a$ and $\Sigma 7m$ GB simulation cells in the presence of single substitutional dopants of different types. The density of states of the undoped boundary is shaded in gray. Panel (a) shows the states near the VBM and panel (b) the states near the CBM. The dashed line is proportional to the projected DOS of α-Al_2O_3 in the "bulk" region of the GB cell, far from the GB. The VBM in the bulk region is indicated by the thin vertical line. For legibility, the bulk DOS is normalized to a lower level than the other curves.

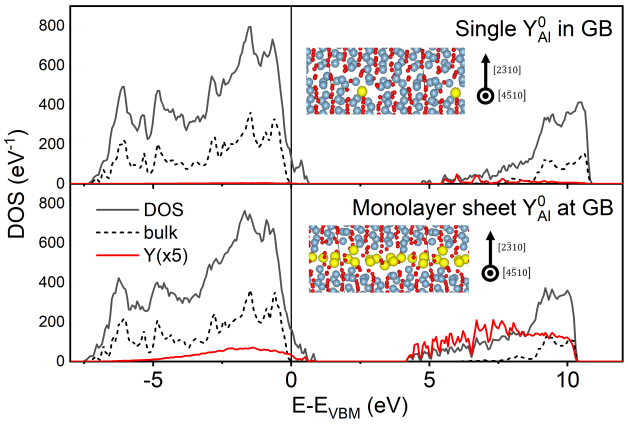


FIG. 5. Densities of states of the $\Sigma 7a$ unit cell with a single Y^0_{Al} substitutional defect and with 87.5% of a monolayer of Y^0_{Al}. The dashed lines show the DOS in the bulk region of the simulation cell and the red lines show the Y-projected DOS, magnified five times for legibility. The structures of the GBs are pictured in the insets, with the Y sites highlighted in yellow. For legibility, the DOS of the bulk region is normalized to a lower level than the other curves.

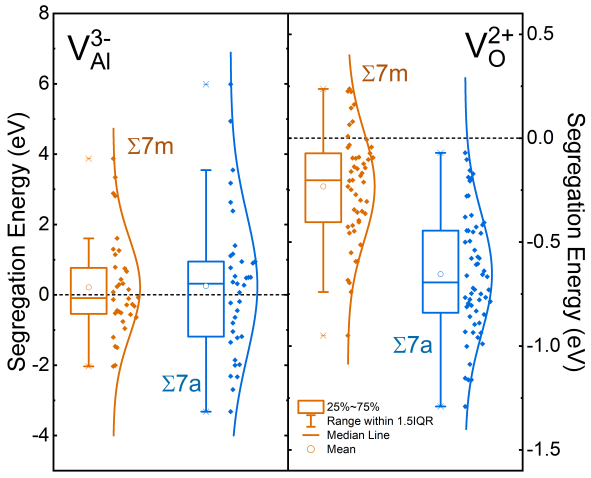


FIG. 6. Distributions of segregation energies of V^{3-}_{Al} and V^{2+}_{O} vacancies at $\Sigma 7a$ and $\Sigma 7m$ GBs.

are likely to segregate, but at concentrations considerably below a monolayer. In contrast, most if not all of the oxygen sites on both GBs have negative V^{2+}_{O} segregation energies and bind oxygen vacancies strongly. The distributions of vacancy segregation energies of both species are roughly normal in both GBs, with no structure suggesting the presence of qualitatively different types of GB site or region. The vacancy segregation energies range from approximately -4eV to 6eV for V^{3-}_{Al} and from approximately -2eV to 0eV for V^{2+}_{O}.

In contrast to V^{3-}_{Al}, where the average segregation energies were similar for both boundaries, V^{2+}_{O} vacancies segregate much more strongly to the $\Sigma 7a$ boundary than to the $\Sigma 7m$ boundary. It is instructive to remember that, although we take the two GB structures considered here

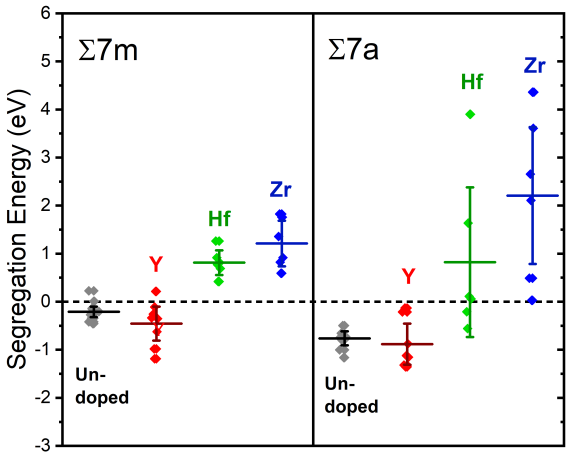


FIG. 7. V_O^{2+} segregation energies at oxygen sites coordinated to substitutional RE dopant sites and at the corresponding oxygen sites in the undoped GB. The vertical bars are 95% confidence intervals.

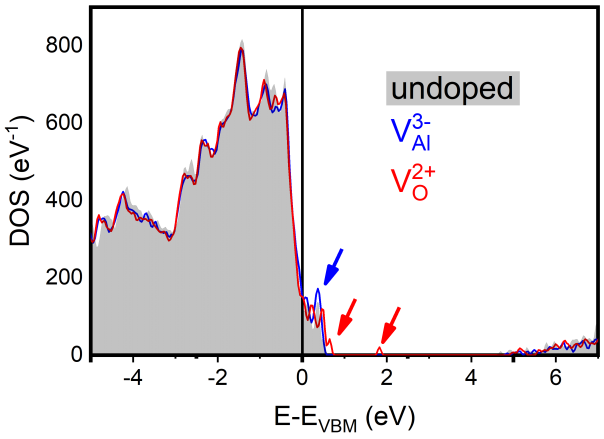


FIG. 8. DOS of the $\Sigma 7a$ GB with V_{Al}^{3-} (blue) and V_O^{2+} (red) vacancies. The near-VBM and gap states of each defect are indicated by arrows. The undoped GB DOS (gray, shaded) is shown for comparison.

as representative of GBs in α-Al_2O_3, experiment shows that the GB diffusivities of oxygen in α-Al_2O_3 bicrystals vary widely [39], suggesting that the diffusivity is strongly dependent on the structure of the GB plane. In particular, the oxygen diffusivity along the $\Sigma 7a$ boundary, with GB plane $(2\bar{3}10)$, is of order a hundred times higher than along the $\Sigma 7m$ boundary, with GB plane $(4\bar{5}10)$. That this experimental distinction is reflected so clearly in our calculated segregation energies is consistent with the hypothesis that whatever complex defects are the agents for oxygen diffusivity, they have some V_O^{2+} character.

The difference in vacancy segregation to different GB structures could arise from the degree of order of the GB structures. The more highly ordered $\Sigma 7m$ GBs have a lower diversity of local coordination configurations at Al and O sites. This causes the spread in segregation energy, both for V_O^{2+} and V_{Al}^{3-}, to be lower in $\Sigma 7m$ GBs. The V_O^{2+} segregation energies are generally lower than those of V_{Al}^{3-}. This could be because more O vacancies than Al vacancies are needed to maintain Schottky equilibrium. This tendency is further accentuated in $\Sigma 7a$ GBs, with a higher number of unfavorable O sites receptive to O vacancies.

Figure 7 shows how the presence of REs modifies the V_O^{2+} segregation energies. The figure compares the segregation energies of V_O^{2+} to the sites coordinated to RE substitutional defects in Figure 2 with the segregation energies to the corresponding sites in the undoped simulation cell. The oxygen sites coordinated to RE substitutional sites exhibit an increased spread in vacancy segregation energy, with the largest spread in Hf- and Zr-doped $\Sigma 7a$. Although Y_{Al}^0 subsitutional defects are large, their presence only rarely reduces the tendency of oxygen vacancies to segregate to boundary sites, rather causing a neutral or small attractive effect. On the other hand, Hf_{Al}^+ and Zr_{Al}^+ substitutionals raise the mean vacancy segregation energy, reducing the tendency of V_O^{2+} to segregate to coordinated oxygen sites by approximately 1 eV in the $\Sigma 7m$ boundary and up to 2 eV in the $\Sigma 7a$ boundary. The change in oxygen vacancy segregation energy is likely to be caused by the Coulombic repulsion between the positively charged defects, Hf_{Al}^+/Zr_{Al}^+ (the charges of which are localized near the defect site), and the positively charged oxygen vacancies. The experimental measurements of Wu *et al.* [7], who showed that Hf doping from 100 to 2000 ppm (Hf:Al concentration) slows the GB transport kinetics of oxygen in α-Al_2O_3 by a factor of approximately 3–8, depending on dopant concentration, support this conclusion.

E. Electronic Structure of Vacancies at the GB

We now show that the abundance of V_O^{2+} at the GB, studied in the previous subsection, can influence Al and oxygen transport via its effect on the density of electronic states near the VBM. By a simple determination of vacancy defect states, we can build a picture that links V_O^{2+} abundance to changes in the electronic structure.

The effects of a single oxygen or Al vacancy on the electronic structure of the $\Sigma 7a$ GB are illustrated in Fig. 8 (the $\Sigma 7m$ GB behaves similarly). The vacancy is created at the GB site that yields the lowest total energy of the system. (The set of sites considered is the same as for the RE substitutions discussed in Subsection III D.) The addition of either V_O^{2+} or V_{Al}^{3-} vacancies creates localized electronic states near the bottom of the band gap. For V_{Al}^{3-}, the increase in the DOS is slight and appears ∼0.4 eV above the VBM; for V_O^{2+}, there are new states ∼0.7 eV and ∼1.8 eV above the VBM. The presence of two

localized energy levels reflects the possibility that the oxygen vacancy may adopt two different charge states, depending on the location of the Fermi level. Qualitatively similar behavior was seen by Choi, Janotti, and Van de Walle [40] when studying defects in perfect α-Al_2O_3 crystals.

Grain boundaries must remain charge neutral on average, so the presence of charged Hf^+_{Al} of Zr^+_{Al} substitutionals modifies the concentrations of other charged defects on or near the boundary. We saw in Sec. III D, for example, that the addition of tetravalent substitutionals decreases the concentration of positively charged oxygen vacancies. Since some or all of these oxygen vacancies are presumably incorporated into the complex defects that mediate oxygen transport, this in turn lowers the ability of the GB to transport oxygen atoms across the scale. Futhermore, as Fig. 8 shows, the exclusion of V^{2+}_O vacancies reduces the density of gap states ∼0.7 eV and ∼1.8 eV above the VBM, reducing the density of states available for hole transport, lowering the hole-mediated electronic conductivity and thus the scale growth rate. If, instead, the density of V^{3-}_{Al} had increased on doping with Zr^{4+} or Hf^4, new gap states would have been created ∼0.4 eV above the VBM and the electronic conductivity would have increased, increasing the scale growth rate.

IV. CONCLUSIONS

This study of substitutional defects at α-Al_2O_3 GBs, their influence on the GB electronic structure, and the vacancy and hole segregation effects they cause, has shown that the mechanism of the RE effect depends to some extent on the choice of dopant ion. In hindsight, given that Hf^+_{Al} and Zr^+_{Al} dopants are charged and considerably smaller than Y^0_{Al} dopants, which are electrically neutral, this is unsurprising. The larger Y^0_{Al} substitutionals cause coordination number changes that are much less pronounced in the case of Hf^+_{Al} and Zr^+_{Al} doping, and the charges of the Hf^+_{Al} and Zr^+_{Al} dopants have strong effects on the V^{2+}_O and hole concentrations at GBs.

We have shown that positively-charged Hf^+_{Al} and Zr^+_{Al} substitutionals at α-Al_2O_3 GBs lower the GB populations of oxygen vacancies because of Coulomb repulsion. This in turn reduces the availability of near-VBM defect states, reducing the hole concentration and thus the electronic conductivity. The positive charges of Hf^+_{Al} and Zr^+_{Al} substitutional defects also cause Coulomb-induced band-bending effects, repelling holes directly and further reducing the electronic conductivity. Coulomb repulsion is unimportant when the dopants are charge-neutral Y^0_{Al} substitutionals, but a 87.5% monolayer coverage of Y^0_{Al} at the GB plane nevertheless reduces the electronic density of states at or above the VBM, lowering the hole concentration via the mechanism proposed by Heuer *et al.* [15].

Although we have considered the RE influence on vacancy populations at GBs, we note that the pre-exponentials in the Arrhenius plots of measured GB diffusivities [2, 41] are much too large to be consistent with the idea that GB diffusion is mediated by point-defect hopping, suggesting instead that it involves coordinated rearrangements of large groups of atoms. We think it likely that these rearrangements correspond to the migration of disconnections, which are GB ledge defects of ledge height h and Burgers vector $\mathbf{b}$; the Burgers vector characterizes the long-range strain field and defines the displacement associated with disconnection motion. Disconnections are always present at GBs in polycrystalline α-Al_2O_3 GBs [42] and can take on a greater V^{3-}_{Al} or V^{2+}_O character. However, more work needs to be done to establish their role conclusively.

For all three dopant species, we have shown that the suppression of GB hole conductivity is a likely cause of the RE effect. When the hole concentration is very low, the inward flow of positively charged holes from the scale-gas interface to the scale-metal interface is too small to neutralize the outward flow of positive charge carried by Al^{3+} ions moving from the metal to the scale-gas interface and O^{2-} ions moving from the gas to the scale-metal interface. A voltage builds up across the scale, slowing the ionic transport kinetics until the hole current is able to keep up.

The suppression of the GB V^{2+}_O concentration, and thus the suppression of the concentration of the positively charged disconnections or other complex GB defects that mediate oxygen transport across the scale, also contributes to the RE effect in the case of Hf or Zr doping. For Y doping, the disruption to diffusion paths caused by steric effects and changes in coordination number may be important. Although Hf and Zr doping create an abundance of gap states below the CBM, these are too far from the Fermi energy to affect GB transport. In any case, this work shows that RE "site-blocking" activity is not the only mechanism capable of explaining the decrease in oxidation rate.

A point of doubt concerns the role of Al diffusion, mediated by the vacancy V^{3-}_{Al} or a more complicated GB defect. The double-oxidation experiments of Quadakkers *et al.* [5] in 1991 and Young *et al.* [43] almost twenty years later suggest that Y doping reduces the outward diffusion of Al^{3+} more than the inward diffusion of O^{2-}. We might conjecture that RE doping suppresses outward diffusion of Al^{3+} through another mechanism related to hole conductivity, in addition to its effects on O^{2-}.

ACKNOWLEDGMENTS

The research at CWRU was supported by ONR, Dr. Eric Wuchina, Program Manager, NOOO14-19-12003, respectively. The research at Imperial College was also supported by ONR, Dr. Eric Wuchina, Program Manager, grant NOOO14-18-1-2556. We thank the CWRU High Performance Computing Cluster, especially Dr. E.

M. Dragowsky, and Imperial's Research Computing Service team for invaluable technical advice and training.

[1] D. Naumenko, B. A. Pint, and W. J. Quadakkers, Current Thoughts on Reactive Element Effects in Alumina-Forming Systems: In Memory of John Stringer, Oxid. Met. **86**, 1 (2016).

[2] A. H. Heuer, Oxygen and aluminum diffusion in α-Al_2O_3: How much do we really understand?, J. Eur. Ceram. Soc. **28**, 1495 (2008).

[3] P. Y. Hou, Impurity effects on alumina scale growth, J. Am. Ceram. Soc. **86**, 660 (2003).

[4] A. H. Heuer, T. Nakagawa, M. Z. Azar, D. B. Hovis, J. L. Smialek, B. Gleeson, N. D. Hine, H. Guhl, H. S. Lee, P. Tangney, W. M. C. Foulkes, and M. W. Finnis, On the growth of Al_2O_3 scales, Acta Mater. **61**, 6670 (2013).

[5] W. J. Quadakkers, A. Elschner, W. Speier, and H. Nickel, Composition and growth mechanisms of alumina scales on FeCrAl-based alloys determined by SNMS, Appl. Surf. Sci. **52**, 271 (1991).

[6] W. T. Chen, B. Gleeson, and A. Heuer, Oxidation Behavior of γ'-Ni_3Al-Based Ni–20Al–5Cr Alloys With and Without Reactive Elements Under Different Heating Conditions, Oxid. Met. **92**, 137 (2019).

[7] Q. Wu, H. M. Chan, J. M. Rickman, and M. P. Harmer, Effect of Hf^{4+} Concentration on Oxygen Grain-Boundary Diffusion in Alumina, J. Am. Ceram. Soc. **98**, 3346 (2015).

[8] H. Cheng, H. S. Caram, W. E. Schiesser, J. M. Rickman, H. M. Chan, and M. P. Harmer, Oxygen grain-boundary transport in polycrystalline alumina using wedge-geometry bilayer samples: Effect of Y-doping, Acta Mater. **58**, 2442 (2010).

[9] H. Cheng, S. J. Dillon, H. S. Caram, J. M. Rickman, H. M. Chan, and M. P. Harmer, The effect of yttrium on oxygen grain-boundary transport in polycrystalline alumina measured using Ni marker particles, J. Am. Ceram. Soc. **91**, 2002 (2008).

[10] B. A. Pint and K. B. Alexander, Grain Boundary Segregation of Cation Dopants in α-Al_2O_3 Scales, J. Electrochem. Soc. **145**, 1819 (1998).

[11] C. Wagner, Contribution to the theory of the tarnishing process, Z. Phys. Chem. **B21**, 25 (1933).

[12] J. S. Sheasby and D. B. Jory, Electrical properties of growing alumina scales, Oxid. Met. **12**, 527 (1978).

[13] J. Balmain and A. M. Huntz, Improvement of the application of an electrochemical method for the determination of transport properties of an alumina scale. Part I: Alumina scale on a β-NiAl alloy, Oxid. Met. **45**, 183 (1996).

[14] J. Balmain and A. M. Huntz, Improvement of the Application of an Electrochemical Method for the Determination of Transport Properties of an a-Alumina Scale. Part II : Influence of Yttrium and Palladium on Alumina Scales Developed on a β-NiAl Alloy, Oxid. Met. **46**, 213 (1996).

[15] A. H. Heuer, M. Zahiri Azar, H. Guhl, M. Foulkes, B. Gleeson, T. Nakagawa, Y. Ikuhara, and M. W. Finnis, The Band Structure of Polycrystalline Al_2O_3 and Its Influence on Transport Phenomena, J. Am. Ceram. Soc. **99**, 733 (2016).

[16] J. Wei, T. Ogawa, B. Feng, T. Yokoi, R. Ishikawa, A. Kuwabara, K. Matsunaga, N. Shibata, and Y. Ikuhara, Direct Measurement of Electronic Band Structures at Oxide Grain Boundaries, Nano Lett. **20**, 2530 (2020).

[17] E. Schumann, J. C. Yang, M. Rühle, and M. J. Graham, High-resolution SIMS and analytical TEM evaluation of alumina scales on β-NiAl containing Zr or Y, Oxid. Met. **46**, 37 (1996).

[18] P. Fielitz, K. Kelm, R. Bertram, A. H. Chokshi, and G. Borchardt, Aluminium-26 grain boundary diffusion in pure and Y-doped polycrystalline α-alumina, Acta Mater. **127**, 302 (2017).

[19] G. Kresse and J. Hafner, Ab initio molecular dynamics for liquid metals, Phys. Rev. B **47**, 558(R) (1993).

[20] G. Kresse and J. Hafner, Ab initio molecular-dynamics simulation of the liquid-metal-amorphous-semiconductor transition in germanium, Phys. Rev. B **49**, 14251 (1994).

[21] G. Kresse and J. Furthmüller, Efficiency of ab-initio total energy calculations for metals and semiconductors using a plane-wave basis set, Comput. Mater. Sci. **6**, 15 (1996).

[22] G. Kresse and J. Furthmüller, Efficient iterative schemes for ab initio total-energy calculations using a plane-wave basis set, Phys. Rev. B **54**, 11169 (1996).

[23] M. L. Bortz and R. H. French, Optical reflectivity measurements using a laser plasma light source, Appl. Phys. Lett. **55**, 1955 (1989).

[24] M. E. Innocenzi, R. T. Swimm, M. Bass, R. H. French, A. B. Villaverde, and M. R. Kokta, Room-temperature optical absorption in undoped α-Al_2O_3, J. Appl. Phys. **67**, 7542 (1990).

[25] K. Kim and K. D. Jordan, Comparison of Density Functional and MP2 Calculations on the Water Monomer and Dimer, J. Phys. Chem. **98**, 10089 (2002).

[26] P. J. Stephens, F. J. Devlin, C. F. Chabalowski, and M. J. Frisch, Ab Initio Calculation of Vibrational Absorption and Circular Dichroism Spectra Using Density Functional Force Fields, J. Phys. Chem. **98**, 11623 (2002).

[27] Y. Wang and J. P. Perdew, Correlation hole of the spin-polarized electron gas, with exact small-wave-vector and high-density scaling, Phys. Rev. B **44**, 13298 (1991).

[28] J. P. Perdew, K. Burke, and M. Ernzerhof, Generalized Gradient Approximation Made Simple, Phys. Rev. Lett. **77**, 3865 (1996).

[29] J. P. Perdew, K. Burke, and M. Ernzerhof, Errata: "Generalized Gradient Approximation Made Simple" [Phys. Rev. Lett. 77, 3865 (1996)], Phys. Rev. Lett. **78**, 1396 (1997).

[30] J. P. Perdew, M. Ernzerhof, and K. Burke, Rationale for mixing exact exchange with density functional approximations, J. Chem. Phys. **105**, 9982 (1996).

[31] C. Adamo and V. Barone, Toward reliable density functional methods without adjustable parameters: The PBE0 model, J. Chem. Phys. **110**, 6158 (1999).

[32] J. Heyd, G. E. Scuseria, and M. Ernzerhof, Hybrid functionals based on a screened Coulomb potential, J. Chem. Phys. **118**, 8207 (2003).

[33] J. Heyd and G. E. Scuseria, Efficient hybrid density functional calculations in solids: Assessment of the Heyd–Scuseria–Ernzerhof screened Coulomb hybrid functional, J. Chem. Phys. **121**, 1187 (2004).

[34] J. Heyd, G. E. Scuseria, and M. Ernzerhof, Erratum: "Hybrid functionals based on a screened Coulomb potential" [J. Chem. Phys. 118, 8207 (2003)], J. Chem. Phys. **124**, 219906 (2006).

[35] A. V. Krukau, O. A. Vydrov, A. F. Izmaylov, and G. E. Scuseria, Influence of the exchange screening parameter on the performance of screened hybrid functionals, J. Chem. Phys. **125**, 224106 (2006).

[36] J. Han, S. L. Thomas, and D. J. Srolovitz, Grain-Boundary Kinetics : A Unified Approach, Prog. Mater. Sci. **98**, 386 (2018).

[37] R. D. Shannon, Revised effective ionic radii and systematic studies of interatomic distances in halides and chalcogenides, Acta Crystallogr. Sect. A **32**, 751 (1976).

[38] T. Futazuka, R. Ishikawa, N. Shibata, and Y. Ikuhara, First-principles calculations of group IIA and group IV impurities in α-Al_2O_3, Phys. Rev. Mater. **4**, 073602 (2020).

[39] T. Nakagawa, H. Nishimura, I. Sakaguchi, N. Shibata, K. Matsunaga, T. Yamamoto, and Y. Ikuhara, Grain boundary character dependence of oxygen grain boundary diffusion in α-Al_2O_3 bicrystals, Scr. Mater. **65**, 544 (2011).

[40] M. Choi, A. Janotti, and C. G. Van De Walle, Native point defects and dangling bonds in α-Al_2O_3, J. Appl. Phys. **113**, 044501 (2013).

[41] J. H. Harding, K. J. Atkinson, and R. W. Grimes, Experiment and theory of diffusion in alumina, J. Am. Ceram. Soc. **86**, 554 (2003).

[42] A. H. Heuer and M. Zahiri Azar, A disconnection mechanism of enhanced grain boundary diffusion in Al_2O_3, Scr. Mater. **102**, 15 (2015).

[43] D. J. Young, D. Naumenko, L. Niewolak, E. Wessel, L. Singheiser, and W. J. Quadakkers, Oxidation kinetics of Y-doped FeCrAl-alloys in low and high pO_2 gases, Mater. Corros. **61**, 838 (2010).